JOURNAL OF THERMOPHYSICS AND HEAT TRANSFER
Vol. 22, No. 4, October–December 2008

Influence of Spanwise Pitch on Local Heat Transfer for Multiple Jets with Crossflow

Vadiraj V. Katti* and S. V. Prabhu†
Indian Institute of Technology, Bombay, Mumbai 400 076, India

DOI: 10.2514/1.35737

The influence of spanwise jet-to-jet spacing on local heat transfer distribution due to multiple impinging circular air jets from an in-line rectangular array on a surface parallel to the jet plate is studied experimentally. The length-to-diameter ratio of the nozzles of the jet plate is 1.0. The flow, after impingement, is constrained to exit in one direction from the confined passage formed between the jet plate and the target plate. Mean jet Reynolds numbers based on the nozzle-exit diameter *d* covered are 3000, 5000, 7500, and 10,000, and jet-to-plate spacings studied are *d*, 2*d*, and 3*d*. Spanwise pitches considered are 2*d*, 4*d*, and 6*d*, keeping the streamwise pitch at 5*d*. For all configurations, the jet plates have ten spanwise rows in the streamwise direction and six jets in each spanwise row. The flat heat transfer surface is made of thin stainless steel metal foil. Local temperature distribution on the target plate is measured using thermal infrared camera. Wall static pressure on the target plate is measured in the streamwise direction to estimate crossflow velocities and individual jet velocities. Heat transfer characteristics are explained on the basis of flow distribution. A simple correlation is developed to predict the streamwise distribution of the Nusselt number averaged over each spanwise strip resolved to one jet hole as a function of jet-flow and crossflow distributions.

Nomenclature

A	=	area of heater surface, m^2
a_0, a_1, a_2	=	factors of correlation given in Eq. (10)
b_0, b_1	=	factors of correlation given in Eq. (10)
C_d	=	coefficient of discharge
C_p	=	pressure loss coefficient $(P_o - P_a)/0.5\rho V_j^2$
d	=	diameter of the jet, m
G_{act}	=	actual jet mass velocity based on jet-hole area, $kg/s\,m^2$
G_c	=	channel crossflow mass velocity based on channel cross-sectional area, $kg/s\,m^2$
G_{ideal}	=	theoretical jet mass velocity based on jet-hole area, $kg/s\,m^2$
G_j	=	individual jet mass velocity based on jet-hole area, $kg/s\,m^2$
$\bar{G}_j$	=	mean jet mass velocity based on jet-hole area for the array, $kg/s\,m^2$
h	=	heat transfer coefficient, $W/m^2\,K$
k	=	thermal conductivity of the jet fluid, $W/m\,K$
l/d	=	aspect ratio of the nozzle
$\dot{m}_j$	=	mean mass flow rate from the nozzle, kg/s
N_c	=	number of streamwise rows of jets
Nu	=	local Nusselt number (hd/k)
$Nu_{o,\text{multijet}}$	=	stagnation Nusselt number due to a jet in each spanwise row
$Nu_{o,\text{single jet}}$	=	stagnation Nusselt number due to a single jet estimated from the correlation corresponding to the jet-row Reynolds number
$\overline{Nu}_{\text{segment}}$	=	Nusselt number averaged over each segment
$\overline{Nu}_{\text{strip}}$	=	Nusselt number averaged over each spanwise strip resolved to one jet hole
P	=	absolute static pressure at the nozzle exit, Pa
P_a	=	atmospheric pressure, Pa
P_o	=	absolute static pressure in the plenum or at the nozzle inlet, Pa
Pr	=	Prandtl number
Q	=	heater input power, W
q''	=	net heat flux imposed on the target plate, W/m^2
R	=	characteristic gas constant of air, $J/kg\,K$
Re	=	mean jet Reynolds number of flow exiting the nozzle $(4\dot{m}_j/\pi d\mu)$
Re_j	=	individual spanwise-row jet Reynolds number
T_{amb}	=	ambient air temperature, K
T_j	=	reference jet fluid temperature on the target plate, K
T_o	=	plenum air temperature, K
T_w	=	target-plate surface temperature, K
V_j	=	mean jet velocity at the nozzle exit, m/s
x	=	distance in the streamwise direction, m
x_n/d	=	nondimensional streamwise jet-hole spacing
y	=	distance in spanwise direction, m
y_n/d	=	nondimensional spanwise jet-hole spacing
z	=	distance between the nozzle-exit plane and target-plate plane, m
z/d	=	nondimensional distance between the nozzle-exit plane and target-plate plane
β	=	factor defined in Eq. (12)
γ	=	ratio of specific heats
μ	=	coefficient of dynamic viscosity, $Pa \cdot s$
ρ	=	density of air, kg/m^3

Received 18 November 2007; revision received 26 May 2008; accepted for publication 4 June 2008.

*Research Scholar, Mechanical Engineering Department.
†Associate Professor, Mechanical Engineering Department; svprabhu@me.iitb.ac.in (Corresponding Author).

I. Introduction

A SINGLE jet finds its application mostly where highly localized heating or cooling is needed. However, when large surface areas require cooling or heating, multiple-jet impingements are desirable. Multiple jets are formed by a number of individual jets. The characteristics of these are influenced basically by two types of interactions. First, the interference between the adjacent jets can occur before impingement on the surface. This may happen when the distance between the jets is small and/or when the distance between the jet plane and target-plate plane is large. Second, the wall jets formed by the adjacent jets collide on the target surface. Such interactions are possible when the pitch is small and/or when the distance between the jet plane and target-plate plane is small but jet velocity is large. Another parameter that influences multiple-jet impingement cooling in a confined space is the crossflow. Crossflow

is defined as the fluid flow in the direction perpendicular to the impingement flow. The crossflow can be either due to an external flow resource or due to accumulated spent-jet-fluid flow. The spent-jet-fluid flow may be allowed to leave the confined passage either in one direction, two opposite directions, or all directions.

In the selection of a multiple-jet system, all of the relevant parameters are to be chosen so that sufficiently high average heat transfer coefficients are attained with permissible variation in local heat transfer coefficients over the entire surface to eliminate local hot/cold spots. In a gas turbine application, to cool hot components such as the internal wall of turbine blades and combustion-chamber walls using an array of multiple impinging jets, the jet flows are confined in a narrow space.

Detailed literature review on jet-impingement heat transfer is available by Martin [1], Jambunathan et al. [2], and Viskanta [3]. Gardon and Cobonpue [4] reported local distribution of heat transfer coefficients for unconfined multiple-jet square arrays using a heat flow transducer and concluded that a single jet produced higher heat transfer rates than arrays of jets. The effect of crossflow on impingement heat transfer due to one row of jets was studied by Metzger and Korstad [5]. The experimental results for heat transfer due to arrays of multiple-jet impingement with one side exit of spent air and possible correlations were proposed by several investigators [6–12]. The heat transfer characteristics with arrays of circular jets with spent air leaving the passage in one, two opposite, and all directions were compared by Obot and Trabold [13]. In all of these studies [5–13], streamwise distribution of segment-averaged Nusselt numbers were reported, but not the spanwise variations because of the limitations of the apparatus and technique used. Goldstein and Timmers [14] used a transient liquid crystal technique and studied heat transfer characteristics due to a single jet and a row of jets with confined impingement and spent fluid exiting in all directions. Garimella and Schroeder [15] investigated local heat transfer characteristics due to confined multiple-jet impingement from square arrays of four jets and nine jets using a discrete heat source and thermocouple. For staggered arrays of circular jets, San and Lai [16] experimentally predicted the optimum value of pitch for heat transfer for different jet-to-plate distances using a foil heater and thermocouple. Fenot et al. [17] and Brevet et al. [18] used a thin-foil technique and IR camera and studied heat transfer characteristics due to one row of confined multiple impinging jets. Brevet et al. [18] optimized the spanwise pitch on the basis of cooling efficiency estimated per unit area of impingement surface. More recently, liquid crystal thermography was used to study local heat transfer distribution due to impingement of arrays of multiple jets with spent air exiting in one direction [19–23]. The distribution of heat transfer coefficient due to arrays of impinging jets involving an increase in spacing between the jets in the streamwise direction and an increase in jet-hole diameters in the streamwise direction using liquid crystal thermography was studied by Gao et al. [24]. The effect of the streamwise pressure gradient on the local heat transfer distribution due to impingement of arrays of multiple jets with spent air exiting in one direction was investigated by Hebert et al. [25]. The effect of increasing the jet-hole diameters and their spacing in the streamwise direction on the local heat transfer distribution for one streamwise row of jets was studied by Uysal et al [26]. Goodro et al. [27] and Park et al. [28] used a thin-foil technique and IR camera to investigate the effects of Mach number and Reynolds number on heat transfer due to jet-array impingement with one side exit for spent air.

It may be observed from the literature that there is a need to study the effect of jet-to-jet spacing on local distribution of heat transfer coefficients in the streamwise and spanwise directions for different channel heights due to impingement of arrays of multiple jets with spent air exiting in one direction. Hence, the objective of the present work is to investigate the influence of spanwise pitch ($y_n/d = 2, 4,$ and 6) on local distribution of heat transfer coefficients in the streamwise and spanwise directions, keeping streamwise pitch constant ($x_n/d = 5$) at different channel heights ($z/d = 1, 2, 3$). These effects on the jet-flow and crossflow velocity distributions also need to be computed. The distributions of heat transfer coefficients averaged over each spanwise strip resolved to one jet hole are to be studied.

II. Experimental Apparatus

A schematic layout of the test facility is as shown in Fig. 1. Air is supplied to the air plenum of the test section by an air compressor through a calibrated orifice flowmeter. An air filter and a pressure regulator are installed upstream of the orifice flowmeter to filter the air and to maintain the downstream pressure at a desired value. Metered air is supplied to the air plenum through a diffuser. Figure 2 shows the schematic view of the test section. The air plenum, 350×450 mm in cross section and 600 mm long, has two screens in between as flow straighteners. A jet plate is flanged at the exit of the air plenum. The jet plates are made of a 5 mm acrylic sheet with jet holes of 5 mm that are drilled to form a required rectangular array. The number of jets in the streamwise and spanwise directions is chosen, respectively, as 10 and 6, because this pattern is identical to

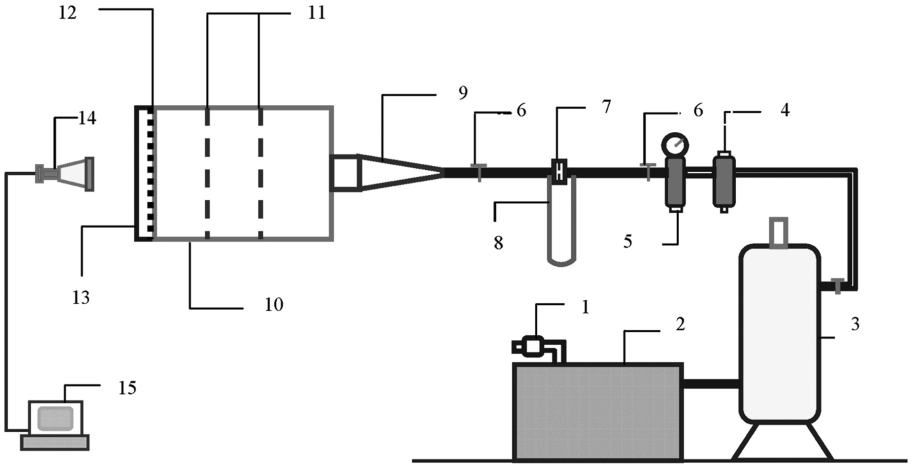

1) Air filter. 2) Air compressor. 3) Air receiver. 4) Air filter. 5) Pressure regulator.

6) Needle valves. 7) Orifice plate. 8) Differential water manometer. 9) Diffuser. 10) Air plenum.

11) Flow straighteners (screens). 12) Jet plate.13) Target plate assembly.

14) Infrared camera. 15) Computer.

Fig. 1 Layout of experimental setup.

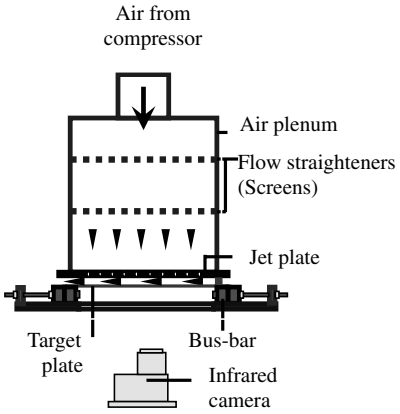

Fig. 2 Test-section assembly.

one of the configurations studied by Florschuetz et al. [11]. The target plate, which also acts as a heater, is made of thin stainless steel foil that is 0.06 mm thick. It is firmly clamped and well stretched between copper bus bars. To minimize the end effects due to a bus bar, an additional length of foil heater of about 65 mm is provided on either side from the end rows of the jet centerlines. Because of the thinness of the foil, lateral conduction is negligible, as reported by Lytle and Webb [29]. One-dimensional energy balance across the heated plate shows that the temperature difference across it is negligibly small. Hence, the local temperature measured on the back surface is considered to be the same as that on the impingement plane.

Thermal images are obtained from an IR camera positioned on the side of the heater opposite the impinging nozzle plate. Hence, the back surface of the heater element is painted black using a thin coat of matte-finish Asian paint, which provides a high-emissivity (0.99) surface. Interchangeable U-shaped spacers are positioned between the jet plate and the target plate and are firmly bolted together with a heater base plate to seal the passage for spent-air flow of jets from three sides. Figure 3 shows the scheme of spent-air flow from the passage between the jet plate and impingement plate and coordinates of the test section. Power is supplied from a regulated dc power source. Voltage taps are soldered at chosen locations on the target plate and wired to a multimeter to measure voltage. The current through the heater plate is directly read from the panel of the dc power source. A Chromel-Alumel thermocouple (K-type) is used to measure the plenum air temperature. The output of the thermocouple is measured by a millivoltmeter. A Thermoteknix Ti200 infrared camera is used to collect the thermal images for the local temperature distribution over the target plate. Supply pressure of the impinging jets is measured as static pressure of the air plenum using a single-leg differential water-tube manometer and a Furness Controls micromanometer (for deflections lower than 20 mm).

A thermal infrared camera reads the temperature of the plate, depending on the emissivity value of the surface of the plate. Therefore, the emissivity of the surface is calibrated and it is found to be equal to 0.99 for the range of temperatures (35 to 70°C)

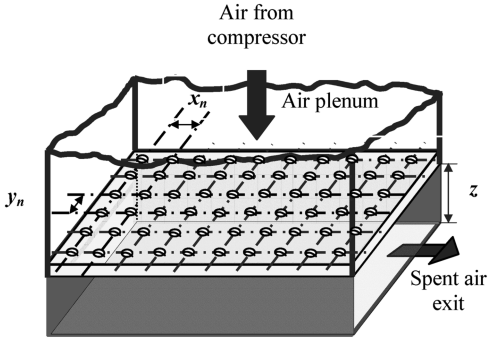

Fig. 3 One-side-exit scheme of spent air from an array of multiple-jet impingement.

Table 1 Configurations studied for the one-side-exit scheme

Streamwise pitch x_n/d	Spanwise pitch y_n/d	Jet-to-plate spacing z/d
5	2	1, 2, 3
5	4	1, 2, 3
5	6	1, 2, 3

investigated. Power-loss estimation from the exposed surface of the heater due to natural convection and radiation is carried out experimentally. The detail procedure is explained by Katti and Prabhu [30]. The corrections are included in the calculations of the Nusselt number to account for heat losses.

The configurations investigated in the present study are shown in Table 1. Each configuration is tested for mean jet Reynolds numbers of 3000, 5000, 7500, and 10,000. The specific geometric configuration is represented in the form x_n/d, y_n/d, and z/d; that is, a configuration convention (5, 4, 2) represents an array of multiple jets with a streamwise pitch of $x_n/d = 5.0$, spanwise pitch of $y_n/d = 4.0$, and jet-to-plate spacing of $z/d = 2.0$.

III. Data Reduction

A. Flow Distribution Estimation

The discharge coefficient for each jet plate is determined from a separate test. The tests are performed with the target plate removed from the test section, and the jets discharge directly to the laboratory environment at atmospheric pressure. The actual mass flow rate is measured from the orifice flowmeter placed upstream of the plenum. The actual mass flux from each jet G_{actual} is estimated from Eq. (1):

$$G_{\text{actual}} = \frac{\text{actual mass flow rate}}{(\pi d^2/4) \times (\text{number of jets})} \tag{1}$$

Supply pressure of the impinging jets is measured as static pressure of the air plenum using a micromanometer. Hence, the ideal flow rate from the jet plate is estimated considering one-dimensional isentropic flow through orifices of the jet plate [Eq. (2)]:

$$G_{\text{ideal}} = P_o \left(\frac{P}{P_o}\right)^{1/\gamma} \left\{ \frac{2\gamma}{\gamma - 1} \left(\frac{1 - (P/P_o)^{(\gamma-1/\gamma)}}{RT_o} \right) \right\}^{1/2} \tag{2}$$

where P and P_o are absolute static pressures at the exit and inlet of the nozzles, and T_o is the absolute plenum air temperature. The jet discharge coefficient is evaluated for different flow rates from Eq. (3):

$$C_d = \frac{G_{\text{actual}}}{G_{\text{ideal}}} \tag{3}$$

The jet discharge coefficient is estimated for a jet Reynolds number ranging from 2000 to 10,000. The mean coefficient of discharge for each of the jet plates of the configurations studied is found to be 0.8.

Static pressure taps (0.5 mm diameter) in the streamwise direction are located midway between spanwise adjacent jets along the centerline of the acrylic target plate of 10 mm thickness. The static jet discharge pressures are used to estimate individual-row jet-flow mass flux G_j:

$$G_j = C_d G_{\text{ideal}} \tag{4}$$

Average jet-flow mass flux $\bar{G}_j$ is the average of all individual-row jet-flow mass fluxes in the streamwise direction. The local channel crossflow mass flux G_c approaching each jet row is summed in the streamwise direction from the second spanwise row until the exit.

B. Heat Transfer Estimation

Target surface temperature measurements for each configuration are made under steady-state conditions using the thermal images collected by infrared camera. The plenum air temperature is used as the reference jet fluid temperature for all heat transfer calculations.

Table 2 Uncertainties of the parameters

Parameter	% uncertainty at $Re = 3000$	% uncertainty at $Re = 10,000$
Temperature	5.0	5.0
Mass flow rate	1.37	1.29
Reynolds number	1.52	1.45
Nusselt number	6.3	5.6
Wall static pressure	0.5	0.5

The local heat transfer coefficients are estimated based on the defining equation

$$h = \frac{q''}{T_w - T_j} \tag{5}$$

where q'' is the net heat flux imposed on the target plate after the heat-loss correction, T_w is the local surface temperature on the target plate, and T_j is the reference jet fluid temperature.

The Nusselt number is computed from Eq. (6):

$$Nu = \frac{hd}{k} \tag{6}$$

Uncertainties in the measurement of different parameters are carried out using the method suggested by Moffat [31] and are listed in Table 2.

Thermal images obtained from infrared camera are digitized using VisIR Ti 200 software. The reference coordinate in the streamwise direction is chosen at a distance of one-half of the streamwise pitch from the centerline of the first spanwise row of jets, toward the closed end of the channel. Contour maps are obtained using MATLAB.

IV. Comparison with Literature

Baseline measurements for Nusselt number distribution are made to validate the experimental setup and procedures. The configuration employed for the baseline tests are similar to the one considered by Florschuetz et al. [11], which simulates cooling of the midchord region of a typical gas turbine blade. This configuration is a rectangular in-line array of jets with a streamwise pitch of $5d$ and spanwise pitch of $6d$ for different jet-to-plate spacings. The passage between the jet plate and the target plate is closed on three sides and the spent air exits only in one direction. Local heat transfer coefficients are estimated using Eq. (5). The local distribution of the Nusselt numbers are averaged segmentwise such that each segment is of $24d$ length in the spanwise direction and of $2.5d$ length in the streamwise direction. Twenty such segments are considered in the streamwise direction. This is done because only segment-averaged Nusselt numbers are reported by Florschuetz et al. as the copper block segments that were used in heat transfer measurements. Figure 4 shows the distribution of segment-averaged Nusselt numbers in the streamwise direction from the present study for $z/d = 1.0$ and 2.0 at a mean jet Reynolds number of 5000. Good agreement between the present results for the measurement of heat transfer distribution and the results presented by Florschuetz et al. is observed. This validates the apparatus and procedure used for the measurement of heat transfer distribution in the present experimentation. However, configuration (5, 4) studied by Florschuetz et al. is also covered during the present investigations and the results show good agreement.

Figure 5a shows the variation in the ratio of individual-row jet mass flux to average jet mass flux of the entire array $G_j/\bar{G}_j$ in the streamwise direction for the (5, 6, 2) configuration. Figure 5b shows the distribution of ratio of local crossflow mass flux to jet mass flux G_c/G_j in the streamwise direction for the (5, 6, 2) configuration. It is observed that the distribution of these two parameters is independent

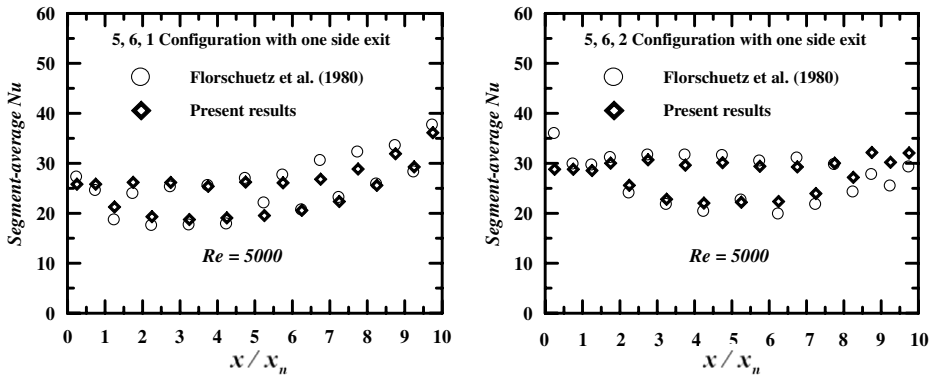

Fig. 4 Comparison of present heat transfer results with those of Florschuetz et al. [11].

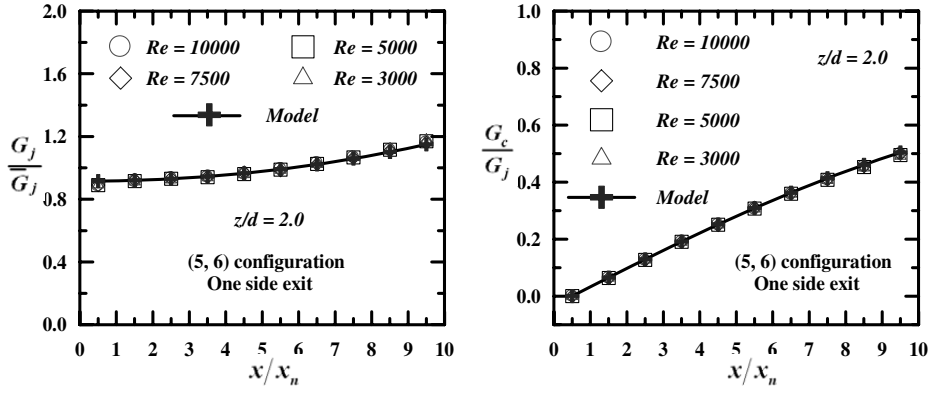

a) Jet-flow distribution **b) Crossflow distribution**

Fig. 5 Comparison of the present flow distribution with the model of Florschuetz et al. [12].

of Reynolds number within the range considered during the present study. The flow distributions are compared with the incompressible one-dimensional flow model suggested by Florschuetz et al. [12] and the results show good agreement. This validates the present method of flow distribution measurement.

V. Results and Discussion

Experiments are conducted at four different mean jet Reynolds numbers of 3000, 5000, 7500, and 10,000. The mean jet Reynolds number is based on jet-hole diameter and average jet mass flux. The channel heights covered are d, $2d$, and $3d$ for all of the configurations investigated. The static pressure measurements in the streamwise direction are made to estimate the amount of mass flow through each row of holes and the amount of crossflow.

A. Flow Distribution

Based on the wall static pressure data, the streamwise distribution of jet mass flux for each spanwise row of jets normalized with mean jet mass flux $G_j/\bar{G}_j$ for the (5, 2), (5, 4), and (5, 6) configurations are shown in Fig. 6 at a mean jet Reynolds number of 10,000 and channel heights of d, $2d$, and $3d$. The distribution of $G_j/\bar{G}_j$ in the streamwise direction represents the variation of relative individual spanwise-row jet Reynolds number Re_j with respect to mean jet Reynolds number Re of the array:

$$\frac{G_j}{G_j} = \frac{Re_j}{Re} \tag{7}$$

$G_j/\bar{G}_j$ distribution for $z/d = 1.0$ is highly nonuniform when compared with those at $z/d = 2.0$ and 3.0. The values of $G_j/\bar{G}_j$ are approximately 0.2, 0.5, and 0.65 for the (5, 2, 1), (5, 4, 1), and (5, 6, 1) configurations at the first row of jets, respectively. The corresponding values at the last row of jets near the channel exit are 2.95, 1.95, and 1.75, respectively. These results indicate that more air is forced to flow through the jet-plate holes near the channel exit than at the upstream row of holes near the closed end or entrance region of the channel. This may be due to the smaller pressure ratios upstream of the channel, indicating less mass of jet fluid issued from the upstream row of jets. But much higher pressure ratios exist toward the channel exit. Hence, a larger mass of jet fluid crosses the downstream rows of jet holes and impinges on the target plate.

The crossflow mass flux G_c for any row is estimated by adding the individual-row jet-flow rates upstream of that row. The parameter G_c/G_jrepresents the crossflow mass flux at any given spanwise row normalized by the corresponding jet mass flux. Figure 7 shows the streamwise distribution of G_c/G_j for different z/d at a mean Reynolds number of 10,000 for all three jet-array configurations: namely, (5, 2), (5, 4), and (5, 6). The values of G_c/G_j increase from zero at the first row of jets to a maximum at the last row of jets near the channel exit. The distribution of G_c/G_j is linear for larger channel heights and higher spanwise pitches. But the distribution becomes nonlinear for narrow channel heights. That is, for $z/d = 1.0$, the distribution of G_c/G_j is highly nonlinear. The nonlinearity increases with the smaller spanwise pitches.

Figure 8 shows the streamwise distribution of jet-crossflow mass flux normalized by mean jet-flow mass flux $G_c/\bar{G}_j$ for different z/d at a mean Reynolds number of 10,000 for all three jet-array configurations. Crossflow velocities increase more rapidly for $z/d = 1.0$ than for $z/d = 2.0$ and 3.0. It is observed that nonlinearity in the crossflow distribution is higher for smaller spanwise pitch and lower channel heights.

It is seen that nonuniformity in the distribution of $G_j/\bar{G}_j$ and nonlinearity in G_c/G_j decrease with increase in the channel cross-sectional area ($y_n/d \times z/d$). The largest channel cross-sectional area is provided by the (5, 6, 3) configuration, for which distribution of $G_j/\bar{G}_j$ is fairly uniform, with a linear distribution of $G_c/G_j$and $G_c/\bar{G}_j$.

B. Local Heat Transfer Distribution

Figure 9 shows the local distribution of streamwise-averaged Nusselt numbers in the spanwise direction for the (5, 4, 1) configuration at $Re = 10,000$ and for the (5, 6, 2) configuration at $Re = 5000$. A good spanwise periodicity is observed for the spanwise distance of four spanwise pitches, excluding two streamwise end rows. Local distributions of heat transfer in the streamwise direction for each channel formed by jets in the spanwise direction are seen to be repetitive. Hence, the local distribution of the Nusselt numbers in the streamwise direction for spanwise locations from $y/y_n = 0$ to 0.5 can be representative of the entire array. A location at $y/y_n = 0$ corresponds to a streamwise line through the jet centerline and $y/y_n = 0.5$ corresponds to a streamwise line midway between two adjacent jet centerlines.

Figure 10 shows the contour maps of local Nusselt number distribution for three spanwise pitches ($y_n/d = 2$, 4, and 6) at $z/d = 1.0$ and 3.0 for a mean jet Reynolds number of 10,000. The maps of local distribution of the Nusselt numbers shown for two streamwise rows confirm their spanwise periodicity. It is observed that the Nusselt number distribution due to the first spanwise row of jets shows a symmetric pattern about the stagnation points because this

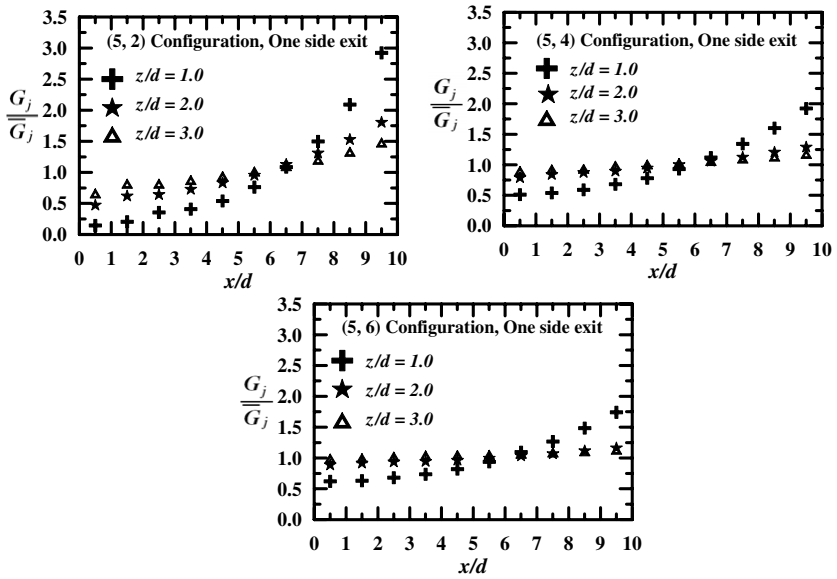

Fig. 6 Streamwise distribution of jet velocities normalized by the mean jet velocity at $Re = 10,000$.

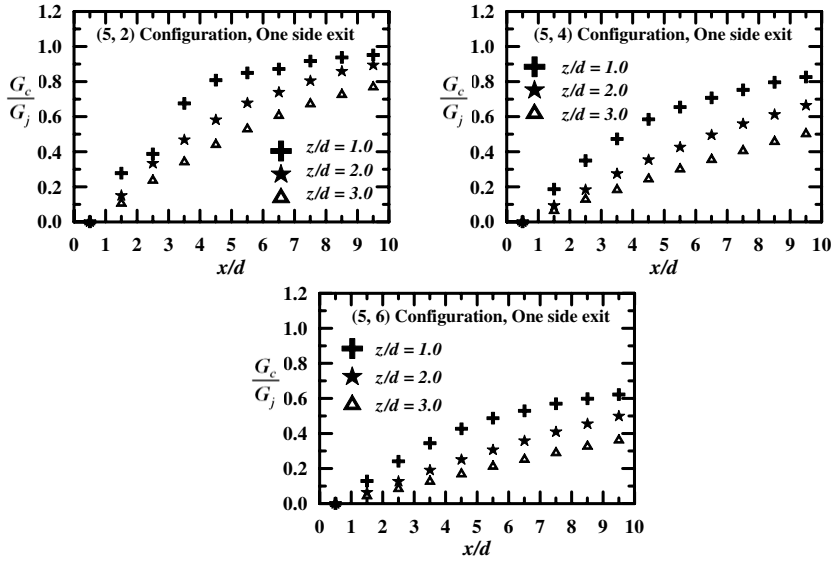

Fig. 7 Streamwise distribution of crossflow velocities normalized by jet velocities $Re = 10,000$.

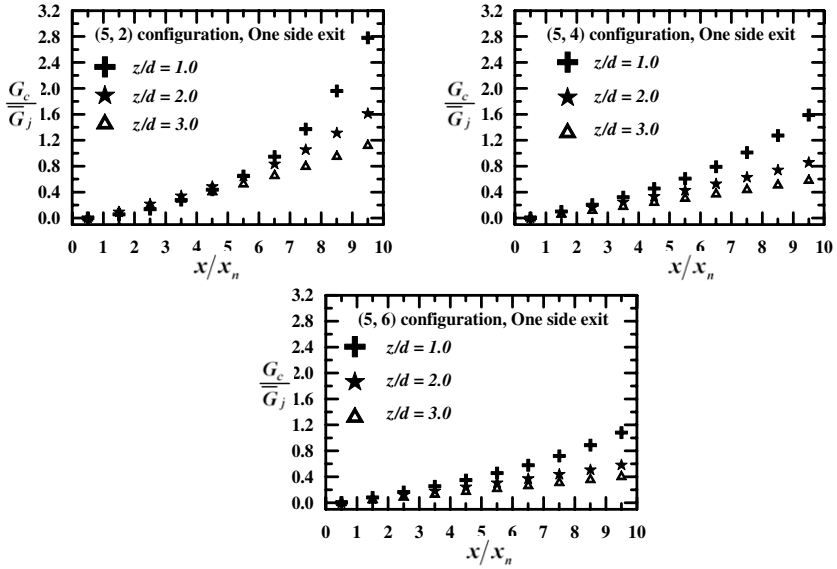

Fig. 8 Streamwise distribution of crossflow velocities normalized by the mean jet velocity at $Re = 10,000$.

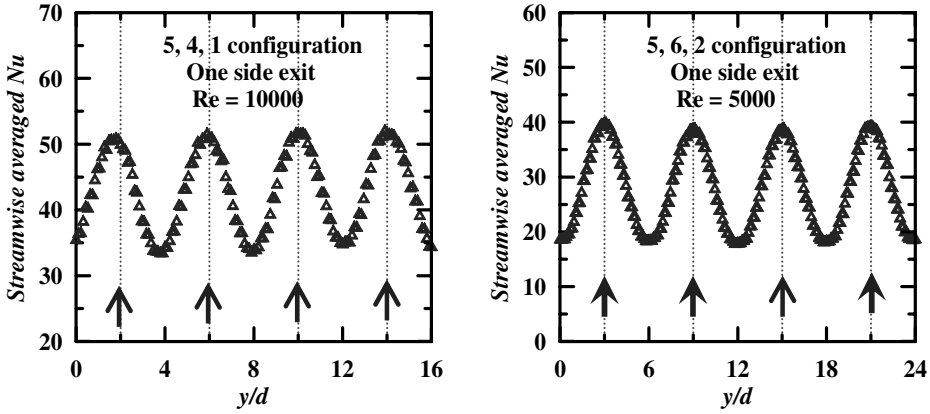

Fig. 9 Streamwise-averaged spanwise distribution of local Nusselt numbers.

row of jets is least affected by the crossflow. But the jets from the second spanwise row onward are influenced by crossflow, and hence the Nusselt number distribution patterns no longer appear symmetric about the stagnation points. The iso-Nusselt-number curves are pushed closer to the stagnation point on the upstream side and are dragged away from the stagnation point on the downstream side. This trend is seen to aggravate toward the channel exit in the streamwise direction. For the narrowest channel ($y_n/d = 2$), the

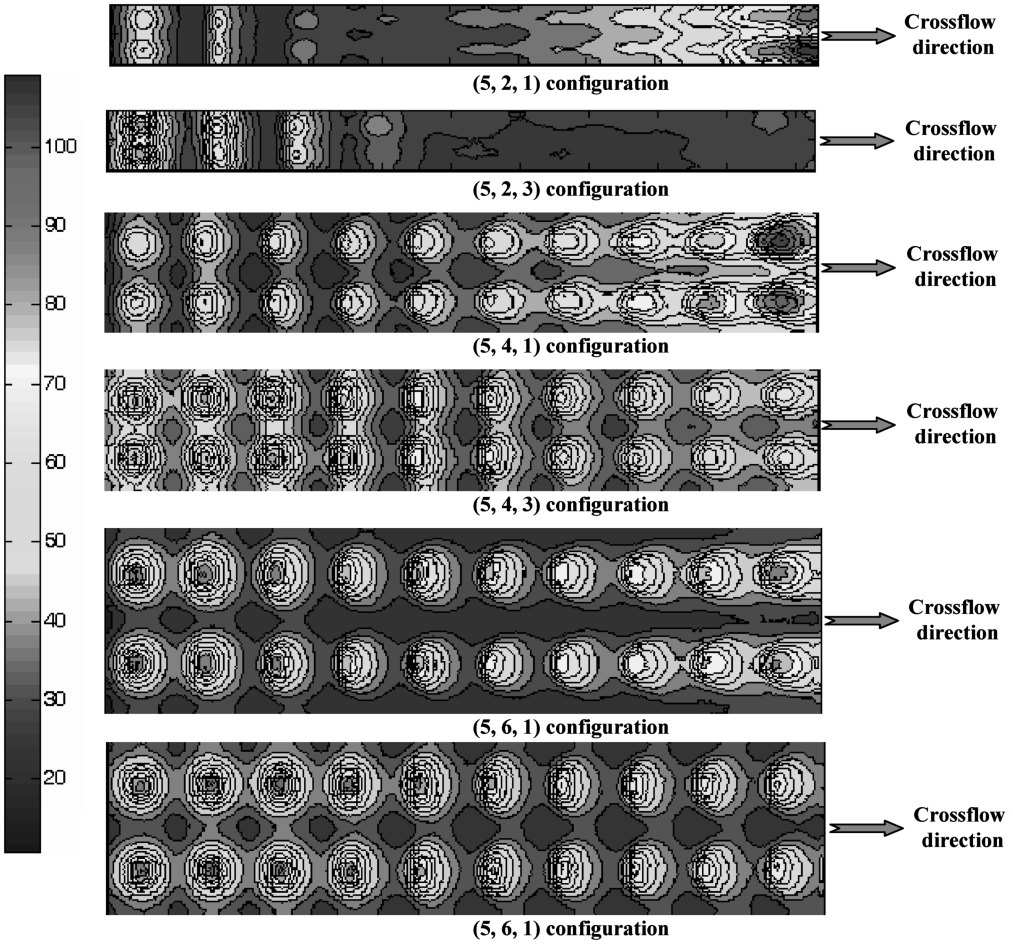

Fig. 10 Contour maps of local Nusselt number distribution at a mean jet Reynolds number of 10,000.

crossflow effects are so high that the heat transfer coefficients tend to be uniform after the third spanwise row of jets. At $z/d = 1.0$, a higher stagnation Nusselt number for the last few spanwise rows of jets is observed. This may be due to higher impinging-jet velocities in this region. Spanwise jet-to-jet interaction decreases with increase in spanwise pitch, which may be visualized from the contour maps.

Figures 11–13 show local distribution of the Nusselt numbers, respectively, for the (5, 2), (5, 4), and (5, 6) configurations at spanwise locations from $y/y_n = 0$ to 0.5 in steps of 0.1 for $z/d = 1.0$, 2.0, and 3.0 and a Reynolds number of 10,000. Spanwise jet-hole row locations relative to the heat transfer surface are indicated by vertical arrows in the figures.

It is observed from Fig. 11 that for the (5, 2) configuration and z/d of 1.0, 2.0, and 3.0, heat transfer coefficients along all lines for $y/y_n = 0$ to 0.5 peak first at $x/d = 2.5$, which corresponds to the centerline of the first spanwise row. These locations indicate the stagnation line of the corresponding spanwise row of jets, which are least influenced by crossflow. However, peak Nusselt numbers are observed to increase with increase in z/d at all y/y_n. At $y/y_n = 0$, stagnation Nusselt numbers at the first spanwise row are approximately 60, 80, and 85 for $z/d = 1.0$, 2.0, and 3.0, respectively. The variation in stagnation Nusselt number can be attributed to higher Reynolds number values for this row of jets with an increase in the channel heights for the same mean jet Reynolds number. Subsequently, in the downstream, all of the spanwise row of jets experience crossflow of spent air from upstream jets. Stagnation points along $y/y_n = 0$ are pushed downstream from the respective jet centerlines. It is seen that stagnation points of the fourth spanwise row in the streamwise direction are shifted by about one-half of the streamwise pitch. However, the minima along this line are pushed more than the peaks in the crossflow direction. The stagnation Nusselt numbers are observed to decrease from the first row to the fourth row and the rate of decrease is higher for higher z/d. However, further downstream for $z/d = 1.0$, Nusselt numbers along $y/y_n = 0$ increase until the flow exits from the channel. The stagnation Nusselt number due to the last spanwise row of jets is about one-and-one-half times the Nusselt number at the stagnation of the first row. But the stagnation points along this line are not distinctly observed from the fifth-row location onward because small variations of the Nusselt number values exist in the direction of crossflow. For $z/d = 2.0$ and 3.0, variations in the streamwise direction almost decay after the fourth spanwise row and Nusselt number distribution is fairly uniform. But a mild gradual increase in Nusselt number values is observed for a channel height of $2d$ from the fifth spanwise row until the channel exit. Along streamwise lines at different y/y_n, patterns of variations are seen similar to those at $y/y_n = 0$. But as one moves from $y/y_n = 0$ to 0.5, the peaks and minima of the Nusselt number distribution are pushed further downstream in the streamwise direction. This may be due to the larger influence of crossflow in this region than along a line through the jet centerline.

Figure 12 shows local distribution of the Nusselt numbers for the (5, 4) configuration at spanwise locations from $y/y_n = 0$ to 0.5 in steps of 0.1 for $z/d = 1.0$, 2.0, and 3.0 and Reynolds numbers of 10,000. It is observed for all z/d of 1.0, 2.0, and 3.0 that heat transfer coefficients along $y/y_n = 0$ peak almost to the same value for the first three spanwise rows in the streamwise direction and their locations almost coincide with jet centerlines. The locations of the Nusselt number peaks represent the stagnation points of corresponding jets. It is again observed that stagnation Nusselt numbers at the first spanwise row of jets increase with z/d. Subsequently, in the downstream for $z/d = 1.0$, stagnation-Nusselt-number values remain almost same for the next two rows, drop a little at the sixth span row, and drop further toward the exit stagnation Nusselt numbers increase gradually for all remaining rows. For $z/d = 2.0$, there is a slight decrease in the stagnation Nusselt numbers for the next five rows, but the values increase for the rows near the exit.

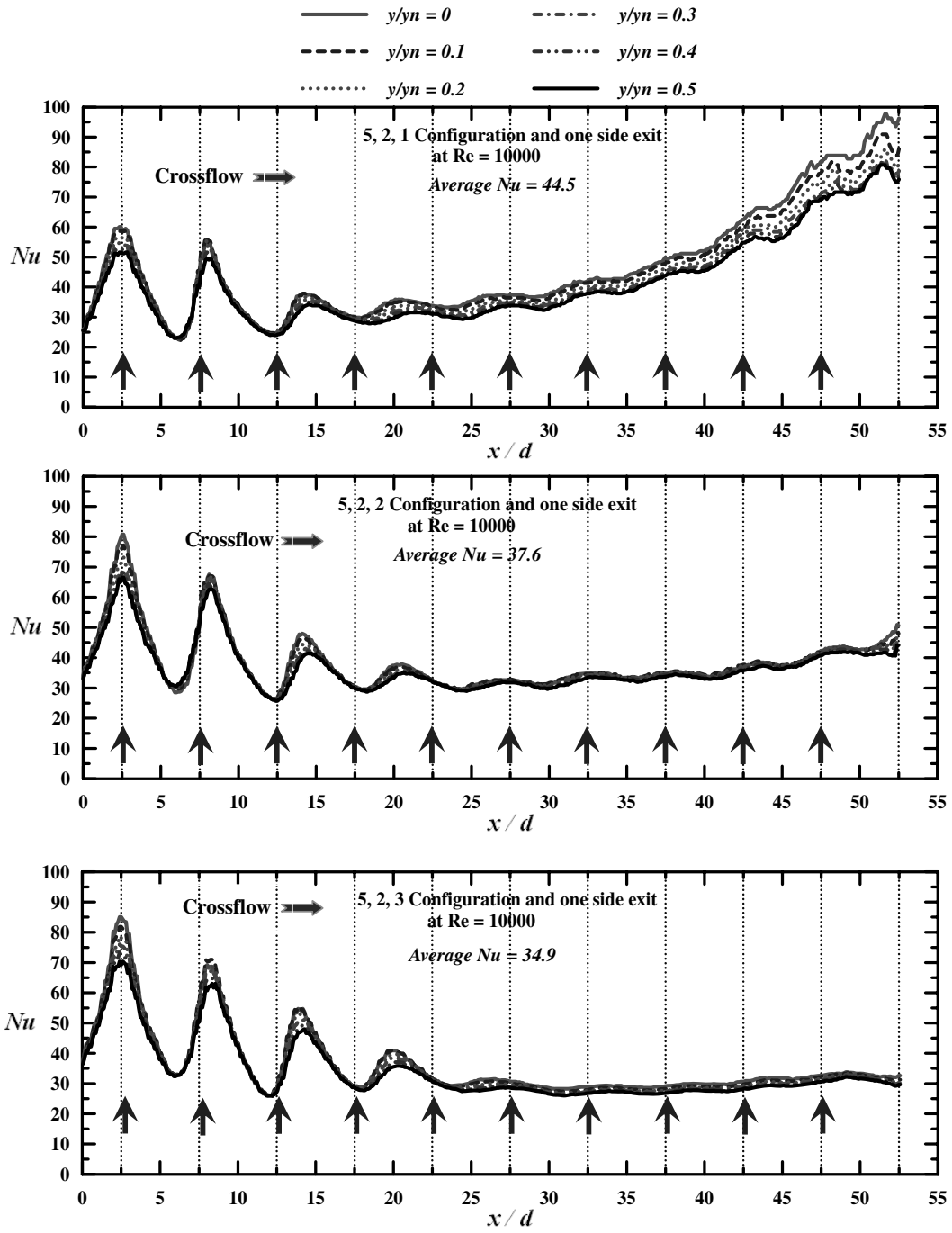

Fig. 11 Streamwise local Nusselt number distribution at different spanwise locations for the (5, 2) configuration with one side exit.

However, for $z/d = 3.0$, stagnation Nusselt numbers gradually decrease until the second-last row, and mild increase is observed for the last row. The locations of the peak Nusselt numbers from the fourth row onward for all z/d do not occur directly under the jet centerline but shift gradually toward the exit. This could be due to sweeping of jets in the downstream because of the crossflow of spent air. It is observed that the peak along this line near the channel exit occurs at $x/d = 50.0$ for $z/d = 1.0$, 2.0, and 3.0. But the corresponding last jet row near the exit is at $x/d = 47.5$. It means the jet issued from the last row impinges on the target plate at a distance of about 0.5 times the streamwise pitch from the axes of the jets.

Similar observations are seen along the lines $y/y_n = 0.1, 0.2, 0.3$, 0.4, and 0.5. The fluctuations of the Nusselt numbers between maximum and minimum decrease from $y/y_n = 0$ to 0.5 at all streamwise locations. In addition, the fluctuation of the Nusselt numbers along the streamwise direction varies with z/d and x/d. It is seen that fluctuations in Nusselt numbers for the first two spanwise rows are almost similar for all three z/d. Subsequently, in the downstream, fluctuations diminish fast along $y/yn = 0.5$ for $z/d = 1.0$, and observations show that the Nusselt number increases more or less linearly toward the exit for the last few spanwise rows. This indicates the dominance of crossflow over jet flow in this region. The fluctuations in Nusselt numbers at $y/y_n = 0.5$ attenuate gradually and almost in the same fashion for other two z/d in the downstream direction until the exit. It is observed that peak Nusselt numbers along the line $y/y_n = 0.5$ are pushed further in the downstream direction from the respective jet centerlines of spanwise rows.

Figure 13 shows local distribution of the Nusselt numbers for the (5, 6) configuration at spanwise locations from $y/y_n = 0$ to 0.5 in steps of 0.1 for $z/d = 1.0$, 2.0, and 3.0 and Reynolds numbers of 10,000. It is observed for all z/d of 1.0, 2.0, and 3.0 that heat transfer coefficients along all lines for $y/y_n = 0$ to 0.5 peak first at $x/d = 2.5$, which corresponds to the centerline of the first spanwise row of jets,

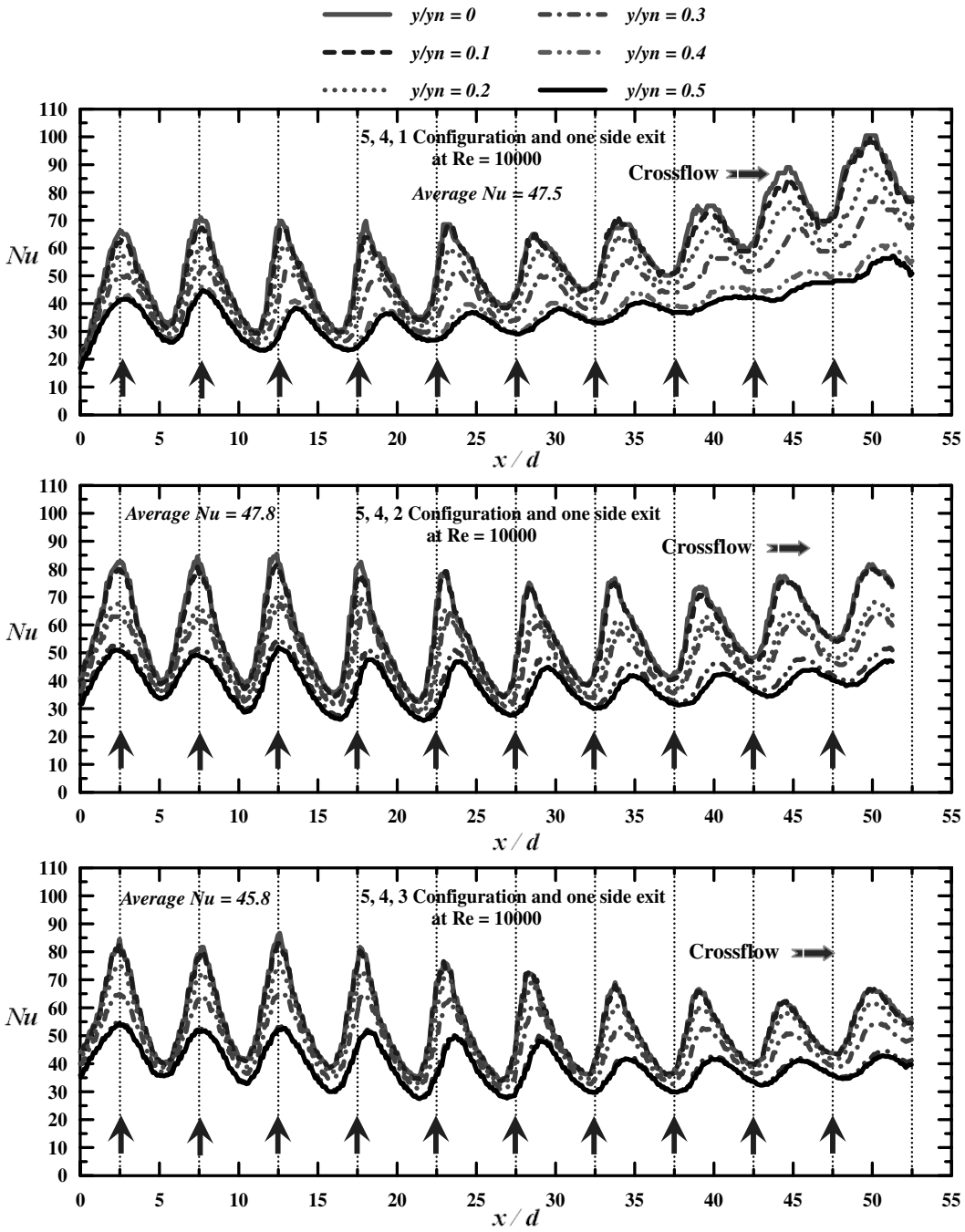

Fig. 12 Streamwise local Nusselt number distribution at different spanwise locations for the (5, 4) configuration with one side exit.

which are least influenced by crossflow. However, stagnation Nusselt numbers are observed to increase slightly with an increase in channel heights at all y/yn. It is observed for all z/d of 1.0, 2.0, and 3.0 that heat transfer coefficients along $y/y_n = 0$ peak almost to the same value for the first three spanwise rows in the streamwise direction, and their locations almost coincide with jet centerlines, similar to the one observed for the (5, 4) configuration. Subsequently, in the downstream for $z/d = 1.0$, peak stagnation-Nusselt-number values drop gradually until the seventh span row. Further toward the exit, stagnation Nusselt numbers increase gradually for the rest of the rows. For $z/d = 2.0$ and 3.0, there is decay in the stagnation Nusselt numbers for all of the rows in the downstream until the exit. The locations of the peak Nusselt numbers from the fourth row onward for all z/d do not occur directly under the jet centerline but shift gradually toward the exit.

Similar observations are seen along the lines $y/y_n = 0.1, 0.2, 0.3, 0.4$, and 0.5. The fluctuations of the Nusselt numbers between maximum and minimum decrease from $y/y_n = 0$ to 0.5 at all streamwise locations. It is seen that fluctuations in Nusselt numbers along $y/y_n = 0.5$ for the first two spanwise rows are almost similar for all three z/d. Subsequently, in the downstream, fluctuations diminish fast for $z/d = 1.0$, and it is seen that the Nusselt number increases more or less linearly toward the exit for the last five spanwise rows. This indicates the dominance of crossflow over jet flow in this region. The fluctuations in Nusselt numbers at $y/y_n = 0.5$ attenuate gradually and almost in the same fashion for the other two z/d in the downstream direction until the exit. It is observed that peak Nusselt numbers along the line $y/y_n = 0.5$ are pushed further in the downstream direction from the respective jet centerlines of spanwise rows.

Although the average Nusselt numbers for all streamwise locations due to the first row of jets are comparable, stagnation Nusselt numbers with a spanwise pitch of $6d$ are higher than with a spanwise pitch of $2d$ and $4d$ for a given z/d. Hence, it is observed that variation of local Nusselt numbers along the spanwise line through the centerline of the first row of jets for a spanwise pitch of $6d$

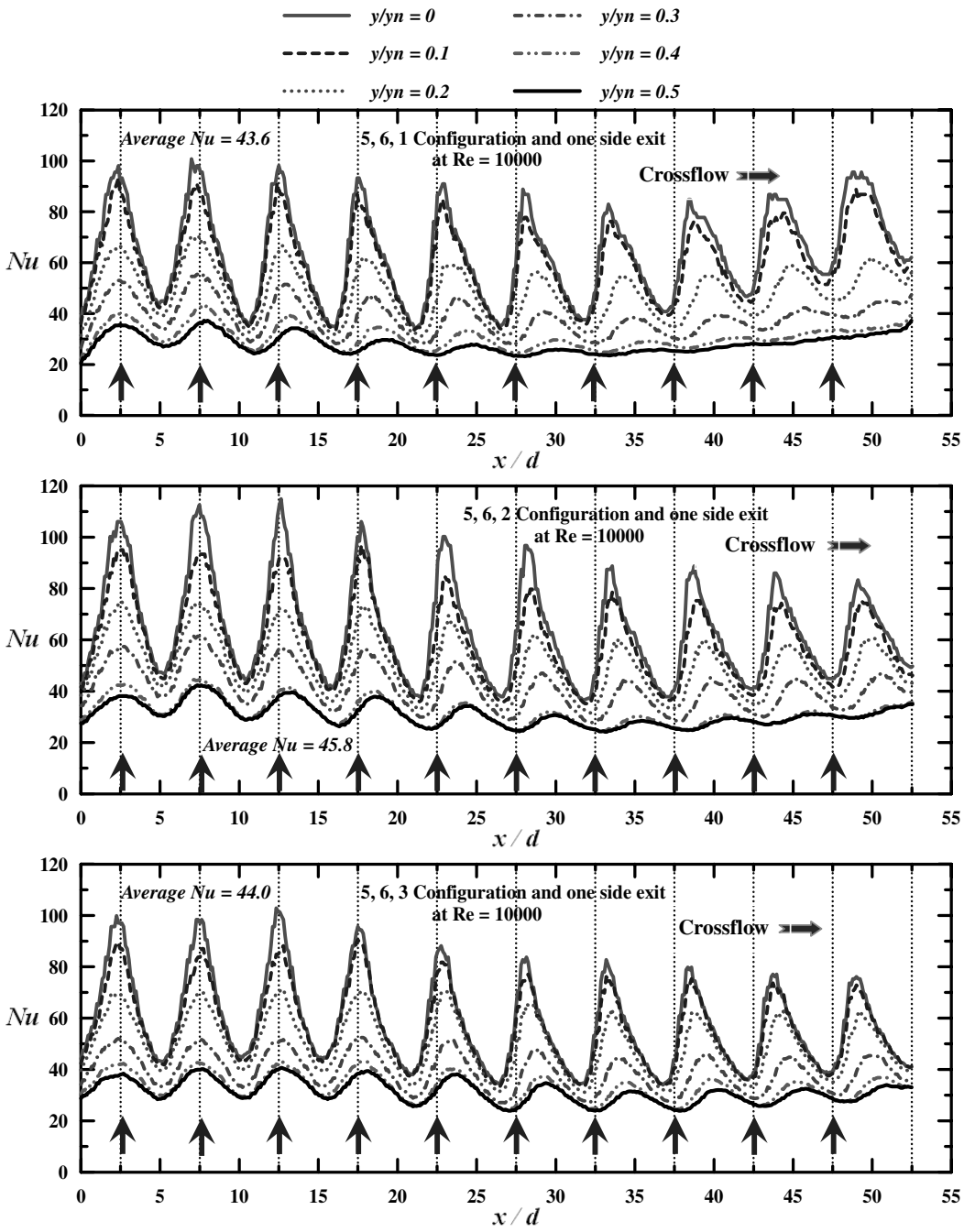

Fig. 13 Streamwise local Nusselt number distribution at different spanwise locations for the (5, 4) configuration with one side exit.

is from 35 to 97, whereas this variation is from 40 to 66 and 50 to 60 for spanwise pitches of $4d$ and $2d$, respectively. This may be due to an increase in the spanwise jet interaction with lower spanwise pitches.

Local heat transfer characteristics on the target plate under an array of jet impingement with spent-air flow exiting in one direction are influenced by the flow characteristics through the channel. Streamwise distribution of local Nusselt numbers along $y/y_n = 0$ depends on the relative influence of impinging-jet velocity and crossflow velocity, and hence it is better understood by the streamwise distribution characteristics of G_c/G_j and $G_j/\bar{G}_j$. Local Nusselt number distribution along $y/y_n = 0.5$ is influenced more by crossflow velocities than individual jet velocities. Hence, linear increase in the local Nusselt numbers for $z/d = 1.0$ in the downstream of the channel along $y/y_n = 0.5$ may be attributed to a sharp increase in $G_c/\bar{G}_j$ distribution, because $G_c/\bar{G}_j$ quantitatively represents the absolute magnitudes of crossflow velocities.

The influence of spanwise pitch on the spread of local Nusselt numbers on the target surface can be understood better from the streamwise distributions of the percentage coefficient of variance (% COV) of local Nusselt numbers. The standard deviations are estimated for each spanwise local Nusselt number and normalized by the respective spanwise-averaged Nusselt number. The % COV is defined as

$$\%\ \mathrm{COV} = 100 \times \frac{\text{standard deviation } \sigma}{\text{spanwise average value } \mu_{\text{span}}} \tag{8}$$

Larger values of % COV of the Nusselt number indicate a higher variation of local Nusselt numbers along a spanwise line at any streamwise location and smaller values of % COV of the Nusselt number signify more uniform distribution along the respective spanwise line. Figure 14 shows the streamwise distribution of % COV of the Nusselt number for the (5, 2), (5, 4), and (5, 6)

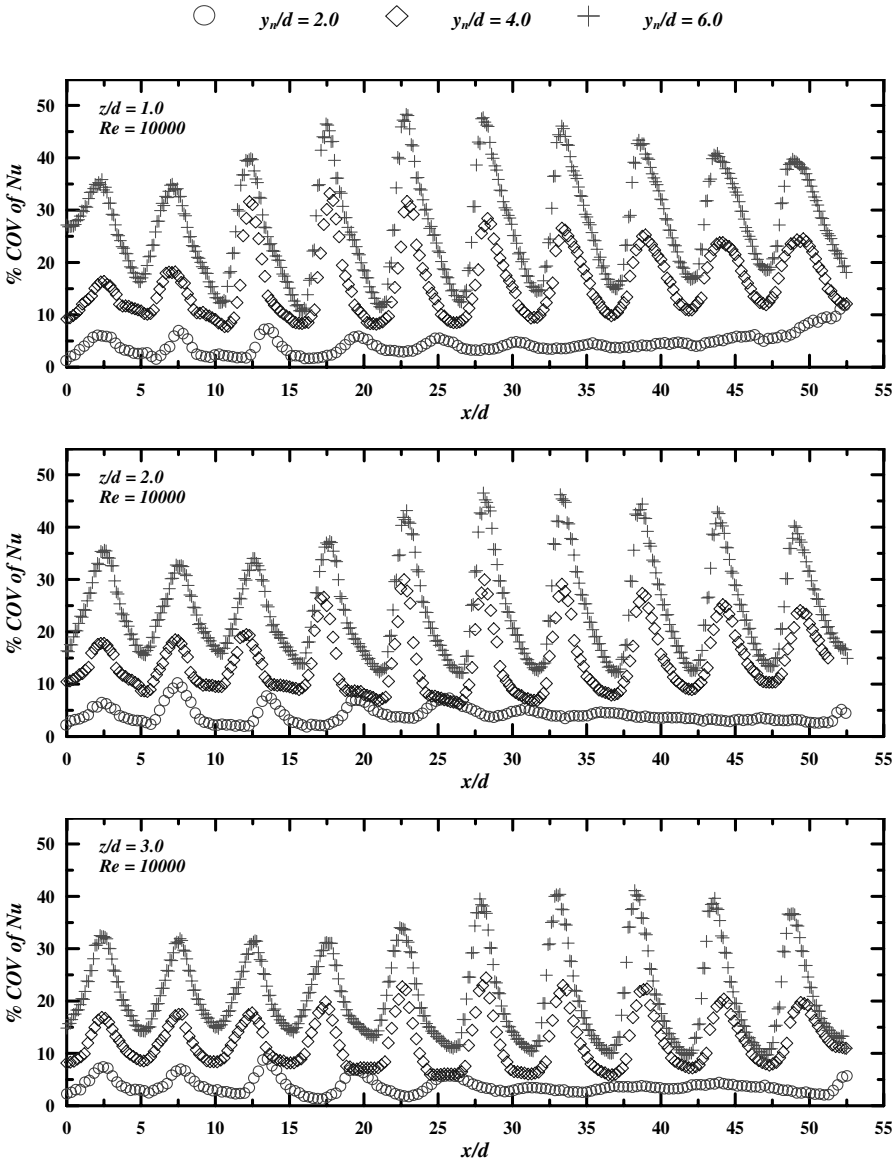

Fig. 14 Influence of spanwise pitch on streamwise distribution of the coefficient of variance of the Nusselt numbers at different channel heights at a mean jet Reynolds number of 10,000 for a streamwise pitch of 5*d*.

configurations at a mean jet Reynolds number of 10,000 and channel heights of d, $2d$, and $3d$. It is observed that the distribution of % COV of the Nusselt numbers is similar to that of the streamwise distribution of local Nusselt numbers. That is, % COV of the Nusselt number values peak almost at the locations of impingement, and minima occur midway between the jets. For all channel heights considered in the present study, % COV of the Nusselt number is higher for larger spanwise pitches at all streamwise locations. This may be due to reduced jet-to-jet interaction on the target surface with larger spanwise pitches. It is seen for $y_n/d = 4.0$ and 6.0 that peak values of % COV of the Nusselt number increase from the third row, fourth row, and fifth row of jets, respectively, for channel heights of d, $2d$, and $3d$. The maximum values of % COV of the Nusselt number are about 48, 45, and 40 for $y_n/d = 6.0$ at $z/d = 1.0$, 2.0, and 3.0, respectively. Corresponding values of % COV of the Nusselt number are about 37, 30, and 25 for $y_n/d = 4.0$. However, for $y_n/d = 2.0$, the maximum values of % COV of the Nusselt number are less than about 10 for all channel heights studied.

C. Comparison of Stagnation Nusselt Numbers from Multiple Jets with Single Jet Estimates

Figure 6 shows the variation of jet mass velocities in the streamwise direction for the (5, 2), (5, 4), and (5, 6) configurations at $z/d = 1$, 2, and 3. Hence, individual Reynolds number at each spanwise row of jets can be computed using Eq. (7). It is of some significance to estimate the stagnation-point Nusselt number due to each spanwise row of jets at the respective Reynolds numbers and jet-to-plate distances using the available empirical correlations for single jet impingement. These estimated values can be compared with stagnation-point Nusselt numbers due to different jet-array configurations. A ratio of $Nu_{o,\text{multijet}}/Nu_{o,\text{single jet}}$ is defined for comparison. $Nu_{o,\text{multijet}}$ is the present experimental value representing the stagnation Nusselt number due to a jet in each spanwise row. $Nu_{o,\text{single jet}}$ is the corresponding stagnation Nusselt number due to a single jet estimated from the empirical correlation at the same individual-row jet Reynolds number and jet-to-plate spacing. The empirical correlations used are reported by Katti and Prabhu [30]. Figure 15 shows the variation of the ratio of $Nu_{o,\text{multijet}}/Nu_{o,\text{single jet}}$ in the streamwise direction for a mean jet Reynolds number of 10,000. Abscissa represents the streamwise jet row number from the closed end of the channel. It is seen that for all three configurations, the value of the ratio decreases gradually in the streamwise direction. The decrease in the value of the ratio is attributed to the influence of crossflow due to impingement of the upstream jets on the impingement of the downstream rows of jets. For all jet-to-plate distances, the decay is seen to be higher for lower spanwise pitches. This may be because of different crossflow

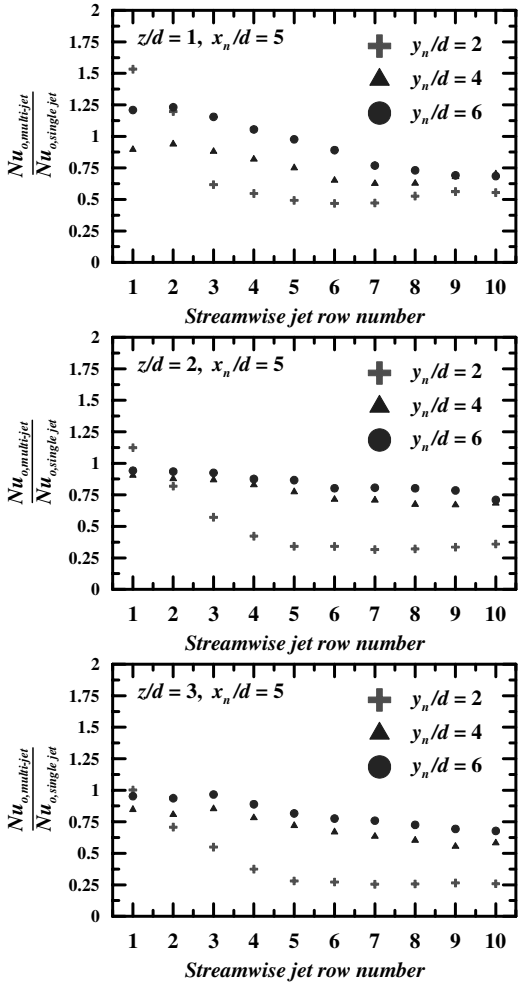

Fig. 15 Comparison of stagnation Nusselt numbers for a row of jets with corresponding single jet values at a mean jet Reynolds number of 10,000.

distribution patterns with different spanwise pitches, even though the streamwise pitch is same. That is, streamwise crossflow distribution tends to become nonlinear with lower spanwise pitches, as seen in Figs. 7 and 8. This trend deteriorates stagnation-point heat transfer coefficients, more significantly observed with the (5, 2) configuration. However, the values of the ratio are higher all along the channel for higher spanwise pitch [i.e., (5, 6) configuration] and may be attributed to the corresponding lower influence of crossflow. The value of the ratio is higher at the first streamwise jet row for all three configurations studied. This may be attributed to the minimum influence of crossflow at the stagnation point due to the first jet row from the closed end of the channel. However, for higher z/d, the ratio slightly drops even at the first jet row. This may be because of higher jet-to-jet interaction caused by higher jet-to-plate distance.

D. Discussion on Average Nusselt Numbers Resolved to One Streamwise Hole Spacing

Figure 16 shows the distribution of the stripwise-averaged Nusselt number in the crossflow direction resolved to one-hole spacing in the streamwise direction for all of the configurations studied at different channel heights. There are ten spanwise rows of jets in the streamwise direction. Hence, ten strips are formed so that strip 1 corresponds to Nu_{strip} due to the first row of jets, strip 2 corresponds to the second row, and so on, in the crossflow direction. Stripwise-averaged Nusselt numbers for $z/d = 1.0$ first decrease and then increase in the downstream for higher Reynolds numbers. But for $Re = 3000$, Nusselt numbers increase in the crossflow direction toward the channel exit for all spanwise pitches studied. The Nusselt numbers increase at a higher rate in the downstream direction with lesser spanwise pitch. With an increase in channel height, Nusselt numbers due to upstream jets increase, whereas the cooling rates decrease due to the row of jets near the channel exit. These effects may be attributed to the fact that in this range of z/d (between 1.0 and 3.0), cooling rates increase with an increase in channel height due to upstream jets because of minimal crossflow. But in the downstream, channel-type flows arise as a result of crossflow and cooling rates vary inversely with channel height.

Correlations are developed for Nusselt numbers averaged to one-streamwise-hole spacing as a function of mean jet Reynolds number, local jet velocity, and crossflow velocity parameters. Hence,

$$\overline{Nu}_{\text{strip}} = f(Re, (G_j/\bar{G}_j), (G_c/G_j)) \tag{9}$$

The least-squares power-function fits are applied and the correlation of the following form is obtained for air as the working fluid:

$$\overline{Nu}_{\text{strip}} = a_o(Re_j^{a_1} Pr^{0.33})\left(\frac{G_j}{\bar{G}_j}\right)^{a_2}\left(1 - b_0\frac{G_c}{G_j}\right)^{b_1} \tag{10}$$

The factors a_0, a_1, a_2, b_0, and b_1 are evaluated from the present experimental data using regression analysis. The factors of correlation are listed in Table 3. The values agree within 10%.

The various parameters of Eqs. (10) can be estimated using the results from the model suggested by Florschuetz et al. [12]. The expressions are as follows:

$$\frac{G_j}{\bar{G}_j} = \frac{\beta N_c \cosh \beta(x/x_n)}{\sinh \beta N_c} \tag{11}$$

$$\beta = \sqrt{2}\left(\frac{\pi}{4}C_d \Big/ \left(\frac{y_n}{d}\times\frac{z}{d}\right)\right) \qquad x = x_n(i-\tfrac{1}{2}) \qquad i = 1,2,3,\ldots,Nc \tag{12}$$

$$\frac{G_c}{G_j} = \left(\frac{1}{C_d\sqrt{2}}\right)\left(\sinh\beta\left(\frac{x}{x_n}-\frac{1}{2}\right)\Big/\cosh\beta\left(\frac{x}{x_n}\right)\right) \tag{13}$$

E. Discussion on Average Nusselt Number for a One-Side-Exit Scheme

The details of average Nusselt numbers for all of the configurations at all Reynolds number and channel heights are given in Table 4. Figure 17 shows the variation of the average Nusselt number of the target surface and pressure loss coefficient C_p across the jet plate for the three configurations at different channel heights for a mean jet Reynolds number of 7500.

Comparisons of average Nusselt number for different channel heights suggest that the (5, 4) configuration performs better than the other two. It is observed that the pressure loss coefficient for the (5, 4) and (5, 6) configurations are comparable and decrease with the channel height. However, for a spanwise pitch of $2d$, pressure loss coefficients are higher at all z/d. This indicates a higher pumping-

Table 3 Correlation factors of Eq. (10)

Configuration	Factors of correlation				
	a_0	a_1	a_2	b_0	b_1
5, 2, 1	0.11	0.74	0.4	0.21	3.5
5, 2, 2	0.09	0.74	0.4	0.27	3.5
5, 2, 3	0.09	0.74	0.8	0.5	2.6
5, 4, 1	0.115	0.71	0.8	0.24	2.4
5, 4, 2	0.043	0.81	0.9	0.27	2.4
5, 4, 3	0.052	0.78	0.9	0.32	2.6
5, 6, 1	0.02	0.9	1.0	0.36	2.0
5, 6, 2	0.033	0.83	1.0	0.3	1.8
5, 6, 3	0.049	0.78	1.0	0.5	2.0

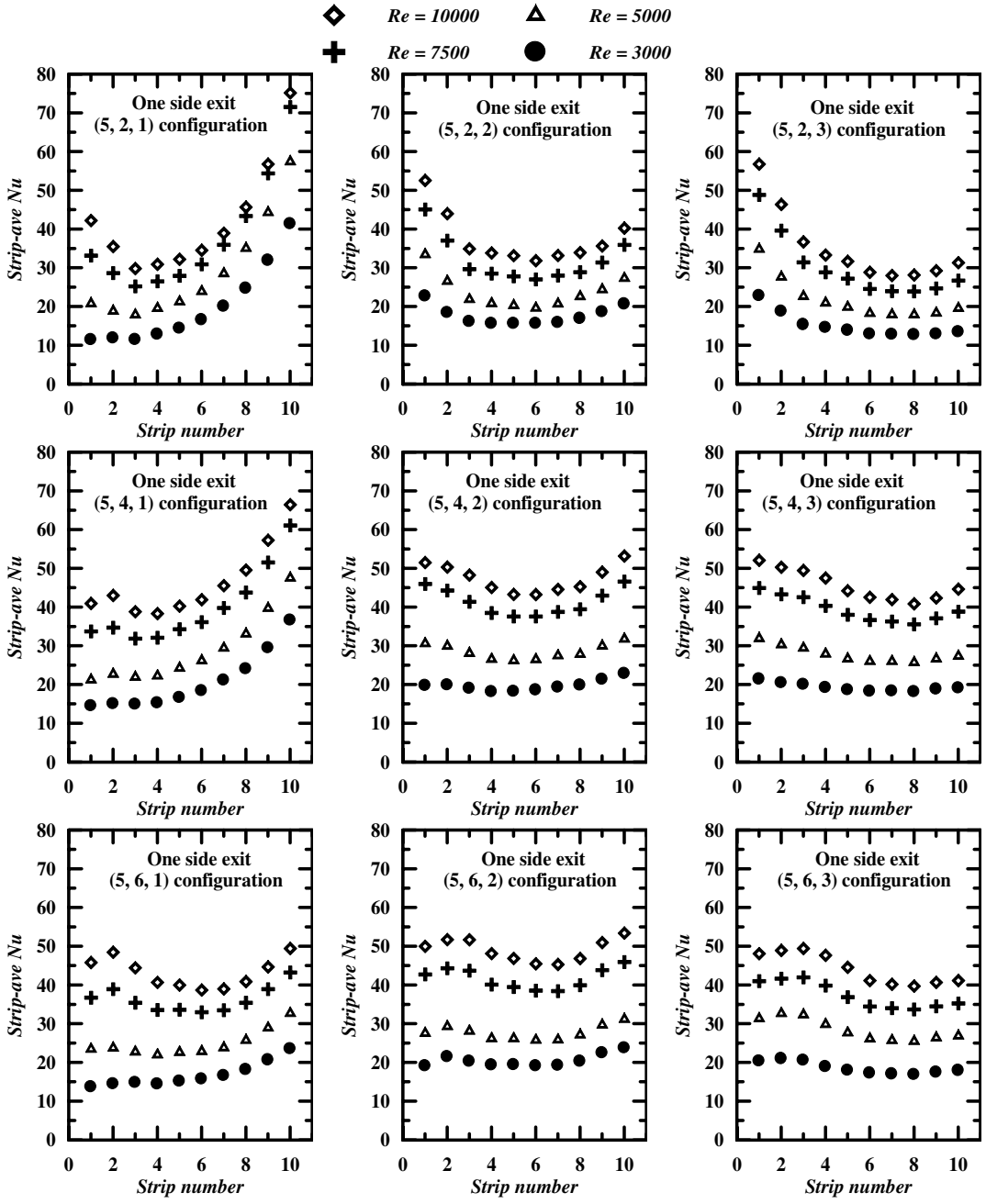

Fig. 16 Distribution of average Nusselt numbers resolved to one-streamwise-hole spacing in the crossflow direction for a streamwise pitch of 5*d* at different channel heights.

Table 4 Average Nusselt numbers for different configurations

			Average Nusselt number at			
x_n/d	y_n/d	z/d	$Re = 3000$	$Re = 5000$	$Re = 7500$	$Re = 10,000$
5	2	1	20.9	30.6	40.0	44.5
5	2	2	17.7	24.0	32.2	37.6
5	2	3	14.9	21.7	29.8	34.7
5	4	1	21.4	29.9	41.2	47.5
5	4	2	19.8	28.7	41.6	47.7
5	4	3	19.3	27.9	39.5	45.8
5	6	1	16.9	25.2	36.6	43.6
5	6	2	17.6	27.9	37.9	45.8
5	6	3	18.5	28.3	37.2	44.0

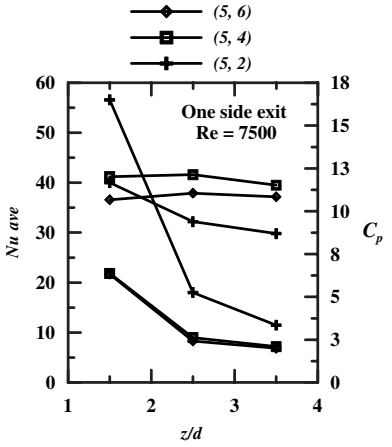

Fig. 17 Variation of the average Nusselt number and pressure loss coefficient.

power requirement for a spanwise pitch of $2d$ than for $4d$ and $6d$ for the same mean jet Reynolds number. Hence, it may be inferred that the (5, 4) configuration cools the target surface with less pumping power than with other two configurations.

VI. Conclusions

Experimental investigation is carried out to study the influence of spanwise pitch on local heat transfer distribution on the target plate due to confined impingement of an in-line rectangular array of multiple jets with spent-air flow exiting in one direction. Spanwise pitches covered are $2d$, $4d$, and $6d$, choosing a constant streamwise pitch of $5d$. Channel heights of d, $2d$, and $3d$ are considered. Mean jet Reynolds numbers studied are 3000, 5000, 7500, and 10,000. The discharge coefficient of the jet plate is determined and hence individual jet velocities and channel crossflow velocities are experimentally estimated.

Conclusions inferred from the present experimental study are as follows:

1) Segment-averaged distribution of the Nusselt number for the (5, 6, 1) and (5, 6, 2) configurations at a Reynolds number of 5000 show good agreement with the reported results of Florschuetz et al. [11] and hence confirms the validation of experimental technique and apparatus.

2) Jet-flow and crossflow distributions for the (5, 6, 1) and (5, 6, 2) configurations at Reynolds numbers from 3000 to 10,000 show good agreement with the flow model suggested by Florschuetz et al. [12] and hence confirm the experimental technique of the measurement of flow distribution. The distributions of nondimensional flow parameters are independent of the Reynolds number.

3) Nonuniformity in the jet flow and nonlinearity in the channel flow increases with a decrease in channel height and spanwise pitch.

4) Local distributions of the Nusselt number in the streamwise direction for each channel formed by jets in the spanwise direction are seen to be repetitive. Hence, local heat transfer characteristics in the streamwise direction studied along streamwise lines, from the one through the jet centers to midway between the jets, can be representative of the entire array.

5) Local distribution of the Nusselt numbers along the streamwise line through the jet centers fluctuates, with peaks occurring for each jet. The fluctuations decay more rapidly for larger channel heights. The values at the peaks increase in the downstream for smaller channel heights ($z/d = 1.0$), but they decrease for larger channel heights ($z/d = 3.0$). The locations of peaks shift toward the downstream from the jet centerline due to crossflow of spent air.

6) Local distribution of the Nusselt numbers along the streamwise line midway between the jet centers fluctuates, with milder peaks occurring for each jet. The fluctuations attenuate rapidly for lower channel heights ($z/d = 1.0$). The values at the peaks increase in the downstream for lower channel heights ($z/d = 1.0$) almost linearly because of increased crossflow velocities in the channel, but they decrease with an increase in channel heights. The locations of peaks shift much further toward the downstream from the jet centerline due to crossflow of spent air.

7) Although the average Nusselt numbers for all streamwise locations due to the first row of jets are comparable, stagnation Nusselt numbers with a spanwise pitch of $6d$ are higher than with spanwise pitches of $2d$ and $4d$ for a given z/d. Spanwise variations in the local heat transfer coefficient at different streamwise lines are larger at higher spanwise pitches. This may be due to an increase in the spanwise jet interaction with lower spanwise pitches.

8) A simple correlation is developed to predict the streamwise distribution of the Nusselt number averaged over each spanwise strip resolved to one jet hole as a function of jet-flow and crossflow distributions.

9) Comparison on the basis of the average Nusselt number and pressure loss coefficient shows that the configuration with a spanwise pitch of $4d$ performs better than $2d$ and $6d$.

Acknowledgment

The authors gratefully acknowledge the Indian Space Research Organization (ISRO), India, for the financial support during this study.

References

[1] Martin, H., "Heat and Mass Transfer Between Impinging Gas Jets and Solid Surfaces," *Advances in Heat Transfer*, Vol. 13, Academic Press, New York, 1977, pp. 1–60.

[2] Jambunathan, K., Lai, E., Moss, M. A., and Button, B. L., "A Review of Heat Transfer Data for Single Circular Jet Impingement," *International Journal of Heat and Fluid Flow*, Vol. 13, No. 2, June 1992, pp. 106–115.
doi:10.1016/0142-727X(92)90017-4

[3] Viskanta, R., "Heat Transfer to Impinging Isothermal Gas and Flame Jets," *Experimental Thermal and Fluid Science*, Vol. 6, No. 2, Feb. 1993, pp. 111–134.
doi:10.1016/0894-1777(93)90022-B

[4] Gardon, R., and Cobonpue, J., "Heat Transfer Between a Flat Plate and Jets of Air Impinging on It," *International Developments in Heat Transfer*, American Society of Mechanical Engineers, New York, 1962, pp. 454–460.

[5] Metzger, D. E., and Korstad, R. J., "Effects of Crossflow on Impingement Heat Transfer," *Journal of Engineering for Power*, Vol. 94, Jan. 1972, pp. 35–41.

[6] Kercher, D. M., and Tabakoff, W., "Heat Transfer by a Square Array of Round Jets Impinging Perpendicular to a Flat Surface Including the Effect of Spent Air," *Journal of Engineering for Power*, Vol. 92, Jan. 1970, pp. 73–82.

[7] Chance, J. L., "Experimental Investigation of Air Impingement Heat Transfer Under an Array of Round Jets," *Tappi*, Vol. 57, No. 6, June 1974, pp. 108–112.

[8] Metzger, D. E., Florschuetz, L. W., Takeuchi, D. I., Behee, R. D., and Berry, R. A., "Heat Transfer Characteristics for Inline and Staggered Arrays of Circular Jets with Crossflow of Spent Air," *Journal of Heat Transfer*, Vol. 101, Aug. 1979, pp. 526–531.

[9] Florschuetz, L. W., Berry, R. A., and Metzger, D. E., "Periodic Stream Wise Variations of Heat Transfer Coefficients for Inline and Staggered Arrays of Circular Jets with Crossflow of Spent Air," *Journal of Heat Transfer*, Vol. 102, Feb. 1980, pp. 132–137.

[10] Florschuetz, L. W., Truman, C. R., and Metzger, D. E., "Stream Wise Flow and Heat Transfer Distributions Jet Array Impingement with Crossflow," *Journal of Heat Transfer*, Vol. 103, May 1981, pp. 337–342.

[11] Florschuetz, L. W., Metzger, D. E., Takeuchi, D. I., and Berry, R. A., "Multiple Jet Impingement Heat Transfer Characteristic—Experimental Investigation of Inline and Staggered Arrays with Crossflow," NASA CR 3217, 1980.

[12] Florschuetz, L. W., Metzger, D. E., and Truman, C. R., "Jet Array Impingement with Crossflow-Correlation of Streamwise Resolved Flow and Heat Transfer Distributions" NASA CR 3373, 1981.

[13] Obot, N. T., and Trabold, T. A., "Impingement Heat Transfer Within Arrays of Circular Jets, Part 1: Effects of Minimum, Intermediate, and Complete Crossflow for Small and Large Spacings," *Journal of Heat Transfer*, Vol. 109, Nov. 1987, pp. 872–879.

[14] Goldstein, R. J., and Timmers, J. F., "Visualization of Heat Transfer from Arrays of Impinging Jets," *International Journal of Heat and*

Mass Transfer, Vol. 25, No. 12, 1982, pp. 1857–1868. doi:10.1016/0017-9310(82)90108-9

[15] Garimella, S. V., and Schroeder, V. P., "Local Heat Transfer Distributions in Confined Multiple Air Jet Impingements," *Journal of Electronic Packaging*, Vol. 123, Sept. 2001, pp. 165–172. doi:10.1115/1.1371923

[16] San, J.-Y., and Lai, M.-D., "Optimum Jet-to-Jet Spacing of Heat Transfer for Staggered Arrays of Impinging Air Jets," *International Journal of Heat and Mass Transfer*, Vol. 44, No. 21, Nov. 2001, pp. 3997–4007. doi:10.1016/S0017-9310(01)00043-6

[17] Fenot, M., Vullierme, J. J., and Dorignac, E., "Local Heat Transfer Due to Several Configurations of Circular Air Jets Impinging on a Flat Plate with and Without Semi-Confinement," *International Journal of Thermal Sciences*, Vol. 44, No. 7, July 2005, pp. 665–675. doi:10.1016/j.ijthermalsci.2004.12.002

[18] Brevet, P., Dejeu, C., Dorignac, E., Jolly, M., Vullierme, J. J., "Heat Transfer to a Row of Impinging Jets in Consideration of Optimization," *International Journal of Heat and Mass Transfer*, Vol. 45, No. 20, Sept. 2002, pp. 4191–4200. doi:10.1016/S0017-9310(02)00128-X

[19] Bailey, J. C., and Bunker, R. S., "Local Heat Transfer and Flow Distributions for Impinging Jet Arrays of Dense and Sparse Extent," American Society of Mechanical Engineers Paper GT-2002-30477, 2002.

[20] Ting Wang, Lin. M., and Bunker, R. S., "Flow and Heat Transfer of Confined Impingement Jets Cooling Using a 3-D Transient Liquid Crystal Scheme," *International Journal of Heat and Mass Transfer*, Vol. 48, Nos. 23–24, Nov. 2005, pp. 4887–4903. doi:10.1016/j.ijheatmasstransfer.2005.04.020

[21] Facchini, B., and Surace, M., "Impingement Cooling for Modern Combustors: Experimental Analysis of Heat Transfer and Effectiveness," *Experiments in Fluids*, Vol. 40, No. 4, Apr. 2006, pp. 601–611. doi:10.1007/s00348-005-0100-y

[22] Esposito, E., and Ekkad, S. V., "Jet Impingement Heat Transfer Visualization Using a Steady State Liquid Crystal Method," *Journal of Heat Transfer*, Vol. 128, Aug. 2006, p. 738. doi:10.1115/1.2221301

[23] Huang, Y., Ekkad, S. V., and Han, J. C., "Detailed Heat Transfer Distributions Under an Array of Orthogonal Impinging Jets," *Journal of Thermophysics and Heat Transfer*, Vol. 12, No. 1, 1998, pp. 73–79.

[24] Gao, L., Ekkad, S. V., and Bunker, R. S., "Impingement Heat Transfer, Part 1: Linearly Stretched Arrays of Holes," *Journal of Thermophysics and Heat Transfer*, Vol. 19, No. 1, Jan.–Mar. 2005, pp. 57–65. doi:10.2514/1.8551

[25] Hebert, R., Ekkad, S. V., Gao, L., and Bunker, R. S., "Impingement Heat Transfer, Part 2: Effect of Streamwise Pressure Gradient," *Journal of Thermophysics and Heat Transfer*, Vol. 19, No. 1, Jan.–Mar. 2005, pp. 66–71. doi:10.2514/1.8588

[26] Uysal, U., Li, P.-W., Chyu, M. K., and Cunha, F. J., "Heat Transfer on Internal Surfaces of a Duct Subjected to Impingement of a Jet Array with Varying Jet Hole-Size and Spacing," *Journal of Turbomachinery*, Vol. 128, Jan. 2006, pp. 158–165. doi:10.1115/1.2101859

[27] Goodro, M., Park, J., Ligrani, P., Fox, M., and Moon, H.-K., "Effects of Mach Number and Reynolds Number on Jet Array Impingement Heat Transfer," *International Journal of Heat and Mass Transfer*, Vol. 50, Nos. 1–2, Jan. 2007, pp. 367–380. doi:10.1016/j.ijheatmasstransfer.2006.06.007

[28] Park, J., Goodro, M., Ligrani, P., Fox, M., and Moon, H.-K., "Separate Effects of Mach Number on Jet Array Impingement Heat Transfer," *Journal of Turbomachinery*, Vol. 129, Apr. 2007, pp. 269–280. doi:10.1115/1.2437774

[29] Lytle, D., and Webb, B. W., "Air Jet Impingement Heat Transfer at Low Nozzle Plate Spacings," *International Journal of Heat and Mass Transfer*, Vol. 37, No. 12, Aug. 1994, pp. 1687–1697. doi:10.1016/0017-9310(94)90059-0

[30] Katti, V. V., and Prabhu, S. V., "Experimental Study and Theoretical Analysis of Local Heat Transfer Distribution Between Smooth Flat Surface and Impinging Air Jet from a Circular Straight Pipe Nozzle," *International Journal of Heat and Mass Transfer*, Vol. 51, Nos. 17–18, 2008, pp. 4480–4495.doi:10.1016/j.ijheatmasstransfer.2007.12.024

[31] Moffat, R. J., "Describing the Uncertainties in Experimental Results," *Experimental Thermal and Fluid Science*, Vol. 1, No. 1, Jan. 1988, pp. 3–17. doi:10.1016/0894-1777(88)90043-X